Less is more: Hollow-truss microlattice metamaterials with dual sound dissipation mechanisms and enhanced broadband sound absorption

Xinwei Li, Xiang Yu, Wei Zhai*

Dr. X. Li, Prof. W. Zhai
Department of Mechanical Engineering, National University of Singapore, 117575, Singapore
E-mail: mpezwei@nus.edu.sg

Prof. X. Yu
Department of Mechanical Engineering, The Hong Kong Polytechnic University, 999077, Hong Kong SAR

Being a lightweight material with high design freedoms, there are increasing research interests in microlattice metamaterials as sound absorbers. However, thus far, microlattices are limited to one sound dissipation mechanism, and this inhibits their broadband absorption capabilities. Herein, as opposed to improving performances via the addition of features, we introduce a new dissipation mechanism subtractively by hollowing out the struts of the microlattice. We then present a conceptually novel class of hollow-truss metamaterial (HTM) that is capable of harnessing dual concurrent dissipation mechanisms from its complex truss interconnectivity and its hollow interior. Experimental sound absorption measurements reveal superior and/or customizable absorption properties in the HTMs as compared to their constitutive solid-trusses. An optimal HTM displays a high average broadband coefficient of 0.72 at a low thickness of 24 mm. Numerically derived, we propose a new dissipation theorem based on the superimposed acoustic impedance of the critically coupled resistance and reactance of the outer-solid and inner-hollow phases, across different frequency bands, in the HTM. Complementary mechanical property studies also reveal improved compressive toughness in the HTMs. This work demonstrates the potential of hollow-trusses, where they

1

gain a new dissipation mechanism through the subtraction of the material and display

excellent acoustic properties.

1. Introduction

The advent of additive manufacturing brings about a new paradigm for materials design –

that being based on structures, as opposed to the materials' chemistry. A new class of

materials, microlattices, manifests from this. Owing to their high degrees of design freedoms

for customizable feature-pore morphology and interconnectivity, microlattices are becoming

the state-of-the-art materials for various applications such as high-strength lightweight

materials,[1-3] energy absorbers,[4-5] electrodes,[6] programmable materials,[7-8] and artificial

bioimplants,[9] etc. Recently, microlattices have also profound research interests for

applications as sound absorbers.

The potential advantages of microlattice sound absorbers over traditional materials

(foams, fabrics, and perforated panels)[10-11] and acoustic metamaterials[12-13] include them

being structurally rigid, robust, customizable, and with the potential for multifunctionality.[14]

However, as compared, the sound absorption performance of microlattices is still limited by

either a narrow bandwidth, low absorption coefficients, or both. Thus far, the mechanisms of

absorption of microlattices lie with either flow resistance or resonance, depending highly on

the architecture and the spatial arrangement of features and their sizes. Representative sound-

absorbing microlattice designs, along with a schematic of their absorption mechanisms, are

illustrated in **Figure 1A**. The presence of a narrow neck, followed by a large cavity, leads to a

Helmholtz resonance behaviour whilst structures with a nearly uniform porosity tend toward

a flow resistance behaviour. For highly-interconnected truss structures consisting of narrow

and wide pores,[15] the sound absorption properties are accurately fitted using Maa's theorem

for multi-layered perforated resonators.[16] Apart from this, there are also structures, designed

to have small pores that precede a large hollow cavity, to specifically achieve such a resonance effect.[15, 17-19] Reminiscent of resonators, the sound absorption coefficient curves of these structures are characterized by the presence of normally-distributed local maximums. In turn, structures that lack distinctly different pore sizes tend to display absorption characteristics closer to foams with an absorption curve monotonically increasing with frequency.[20] These structures include "simpler" truss arrangements, such as the woodpile structure,[21-23] structures with a low strut-to-cell size ratio,[24] and structures highly-open in nature, for instance, the triply periodic minimal surface structures.[25] Sound absorption coefficients for woodpile microlattices are found to be accurately fitted using flow resistance models such as the Johnson-Champoux-Allard-Lafarge model.[21-22] Generally, for structures based on flow resistance, unless the pore sizes are designed to be on a similar length scale as the thickness of the viscous boundary layer,[23] absorption coefficients tend to be hard to achieve unity. Studies have also shown that for the same structure, increasing pore sizes results in the absorption curve deviating away from distinct resonance peaks, saturating to be foam-like.[26] Built on top of the current mechanisms, efforts have been placed to broaden the absorption bandwidth by arranging different cells laterally to achieve a heterogeneous absorber,[17, 27] or by adding cells through-thickness to achieve a functionally-graded absorber.[21-22] However, these methods result in an increased unit absorbing surface, or depth, to achieve the improved performance, and this results in drastically increased microlattice unit sizes. As such, the current sound absorption mechanism of a microlattice is limited to either one of the abovementioned, and a bottleneck is hence faced in attaining better properties. It is apparent that new mechanisms need to be introduced.

Traditionally, to achieve additional functions or enhanced performance, components are often additively added (such as the prior-mentioned heterogeneous, functionally-graded design) to a material. However, additive manufacturing allows the selective reduction of

materials which in turn introduces and/or enhances functionalities.[14] Leveraging this, herein, we introduce an additional sound dissipation mode to truss microlattices by further introducing porosity – in the form of hollowing their struts. Effectively, an additional dissipation mode that is based on the resonance of the geometry, normally observed in acoustic resonators,[28-30] is harnessed and added through the hollow strut interiors. We then present a novel class of hollow-truss metamaterial (HTM) (**Figure 1B**). Experimental sound absorption measurements of digital light processing (DLP) fabricated HTM samples and the numerical analyses of mechanisms reveal superior and/or customizable sound absorption properties with a high dependency on their outer-solid and inner-hollow strut diameters. Numerically derived, a new dissipation mechanism, based on the superimposed path of the critically coupled resistance and mass reactance of the two phases across the frequency bands, is then brought forward. It also serves as a design guideline for HTMs. For an HTM with a set of compatible strut diameters, the average absorption coefficient measures to be 0.72, a drastic increase from its constituents with values of 0.47 and 0.38. The effective bandwidth is also improved, where 90.4% of its absorption coefficients are above a high value of 0.6, as compared to 10.9% and 17.9% of its constituents. Apart from that, complementary studies on compressive properties also reveal superior specific energy absorption improvements in the HTMs. Remarkably, these are achieved via a 68% reduction in mass. These fully substantiate a concept of "less is more", where additional/improved functionalities are gained with the reduction of materials and weight (**Figure 1C**).
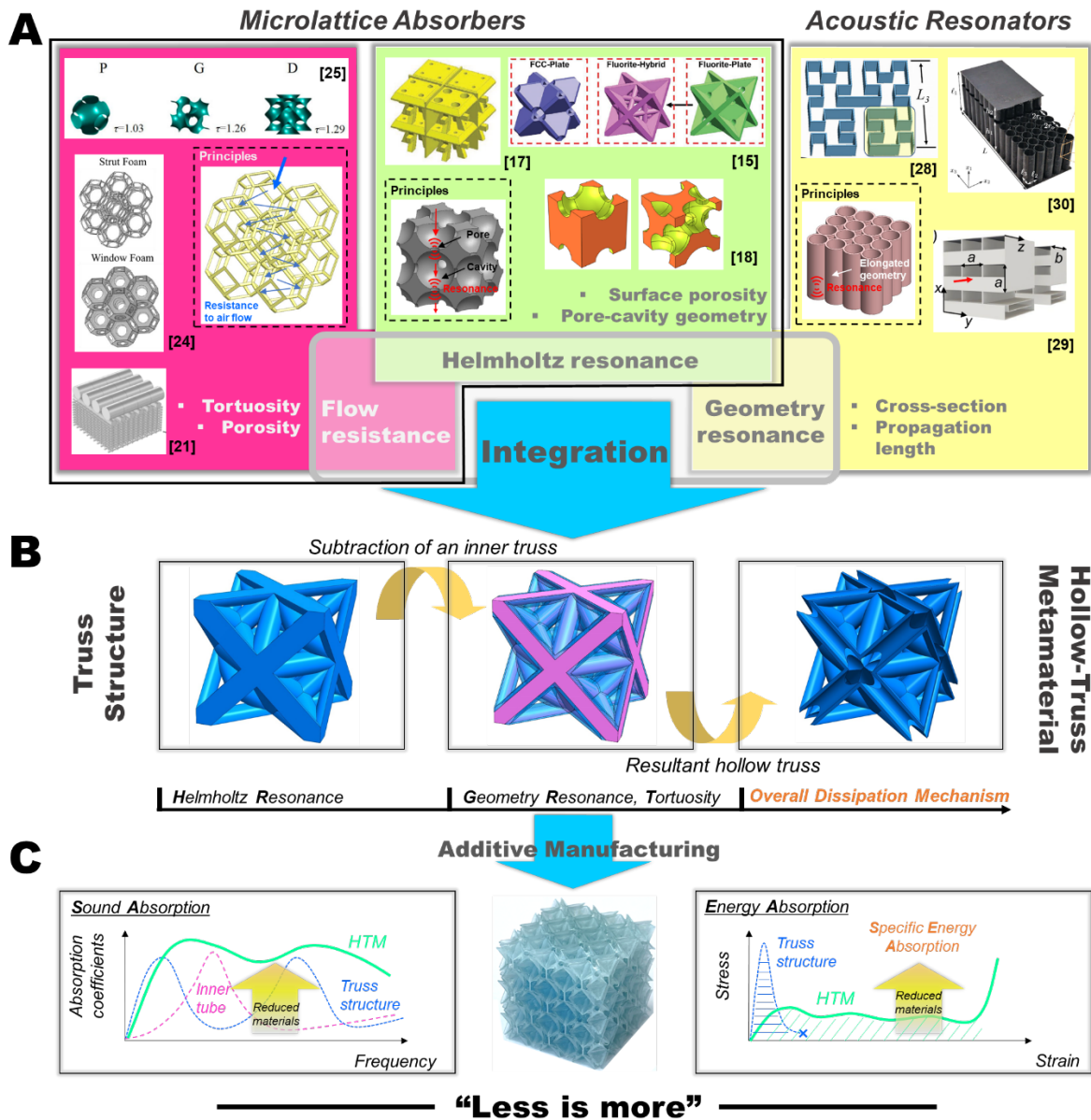
Figure 1: An overall schematic of the design of our hollow-truss metamaterial. (A) Representative illustrations, of the typical sound-absorbing microlattices and their associated mechanisms which are reported in the literature. Their references are labelled in the same figure. References 15 and 17 are reproduced with permission from Wiley. References 18 and 24 are reproduced with permission from Elsevier. References 21 and 28 are reproduced with permission from the American Institute of Physics. Reference 25 is reproduced with permission from Taylor & Francis. References 29 and 30 are reproduced with permission from Springer Nature. (B) A schematic of the design process of the HTM, from the

subtraction of an inner truss to the resultant hollow truss. The figure also shows the additional geometrical resonance on top of the Helmholtz resonance of the solid truss structure. (C) An illustration of an additively manufactured HTM, revealing both improved sound and energy absorption, fully substantiating the concept of "less is more" herein.

2. Results and discussion

2.1 Sound absorption performances

Our starting design is based on a truss arrangement that mimics the fluorite crystal structure. Details of this structure can be found in **Figure S1**, Supporting Information. As shown in **Figure 1B**, the truss microlattice consists of struts edge-joined at the lattice points of the fluorite crystal. The HTM is then achieved by making the microlattice internally hollow by subtracting the same truss structure of a lower strut diameter (**Figure 1B**). Therefore, tubular trusses are obtained as opposed to solid ones. Sound absorption takes place via the dissipation of sound waves through viscothermal losses when they travel through pores or cavities. The magnitude of the loss is directly related to the dimension and geometry of the constituting components, i.e., the solid and hollow strut sizes. Herein, we term the pure solid fluorite truss as the outer-solid truss (OST) and the hollow interior cavity to be the inner-hollow truss (IHT). We have fixed the cubic cell length to be 8 mm; therefore, key parameters only include the OST and IHT strut diameters as schematically illustrated in **Figure 2A**. For instance, the IHT diameter specifies the width of the hollow channel whilst that of the OST determines the size of the structural pores and cavities. A constituent parameter, the wall thickness, is in turn related to the subtraction of the IHT from the OST (**Figure 2A**). To illustrate the contributions of the IHT and OST phases and their trends across a range of strut diameters, the sound absorption properties of the constituent phases are first investigated. Nomenclature is based on their respective acronym, suffixed with their strut diameters in

millimeters. The OST and IHT strut diameters are varied in steps of 0.2 mm, in the range of 1 – 1.6 mm and 0.6 – 1.2 mm, respectively. Their sound absorption coefficient curves, measured using the impedance tube technique, are shown in **Figure 2A**. Resonance peaks in the OST absorption curves are observed to left-shift with respect to frequency with increasing strut diameter and the highest peak is observed for OST-1.4. For OST-1.6, sufficient left-shift has taken place and double peaks are observed. In turn, absorption curves for IHT right-shifts with increasing diameter.

Figure 2B shows a chart that depicts the geometries and studies carried out for the HTMs. The OST and IHT strut diameters of the HTMs are labelled on their respective rows and columns whilst their corresponding percentage reduction in mass from the introduction of the IHT, with respect to the OST, is illustrated in the heat map. For a broad overview of the influence of the HTM geometry on sound absorption properties, herein, we present three types of studies: (i) simultaneously increased OST and IHT diameters whilst keeping a constant wall thickness, (ii) constant IHT with varied OST and wall thickness, and (iii) constant OST with varied IHT and wall thickness. The simultaneously increased OST and IHT diameters allow us to understand the collective influence of the IHT and OST porosities. In turn, a constant OST(IHT) allows us to examine the influence of varying IHT(OST) sizes on the HTM absorption properties. For the constant OST(IHT), additionally, we also investigate different OST(IHT) sizes to understand their extent of influence.

Figure 2C shows the series of sound absorption curves of HTMs with a systematic increment of both the OST and IHT diameters under a constant wall thickness of 0.2 mm. The HTM nomenclature is based on OST/IHT diameters suffixed. For comparison, the absorption curves of their constituents are plotted in the same figure. The most obvious is that the average absorption coefficients generally increase with increasing OST and IHT diameters. Another implication is that the overall absorption curve is a non-trivial

combination of the constituent curves and is highly dependent on the pore sizes. The curves for HTM-1/0.6 and HTM-1.2/0.8 are observed to closely follow that of their constituent OST whilst that for HTM-1.4/1 is based on a "midpoint" of its constituents. Nonetheless, HTM-1.6/1.2 reveals the most effective superposition where the HTM curve shows to be generally much higher than both the OST and IHT throughout.

Figure 2D shows the trends for a constant OST. At a fixed OST-1.6, both the addition and an increasing IHT from 0.8 to 1.2 reveal significant increases in the sound absorption coefficients along with a slight right peak shift. The peak shift is consistent with the IHT trend observed in **Figure 2B**. In turn, no notable differences in the absorption properties are observed for the HTMs consisting of OST-1.2. In fact, the HTM curves follow that of the OST-1.2 closely. This is in contrast to the large variations observed with an OST of 1.6. **Figure 2E** shows the cases for a constant IHT. For both IHT-0.8 and 1.2, observations show that the IHT curves are dissimilar to either of their HTM curves. In other words, the introduction of OST has drastically changed the absorption behaviour and there seems to be a lack of contribution by the IHT. This is in contrast to the cases observed in **Figure 2D** for the OST studies, where the addition of IHT influences the HTM properties whilst still on top of the OST basis. These examples show that the extent of contribution by either phase is highly dependent on the physical geometries of both.

Overall, HTM-1.6/1.2 has the highest improvement in the sound absorption properties over its constituents. Figuratively speaking, the average absorption coefficient of HTM-1.6/1.2 is around 0.72 whilst that for OST-1.6 and IHT-1.2 is at 0.47 and 0.38, respectively. In terms of effective bandwidth, the proportion of its absorption curve above a high coefficient value of 0.6, is around 90.4% for HTM-1.6/1.2, much higher than 10.9% and 17.9% for OST-1.6 and IHT-1.2, respectively. These indicate that the absorption is high

throughout a broad range of frequencies. Remarkably, the increments in properties are achieved with a 68 % reduction in mass from OST-1.6.
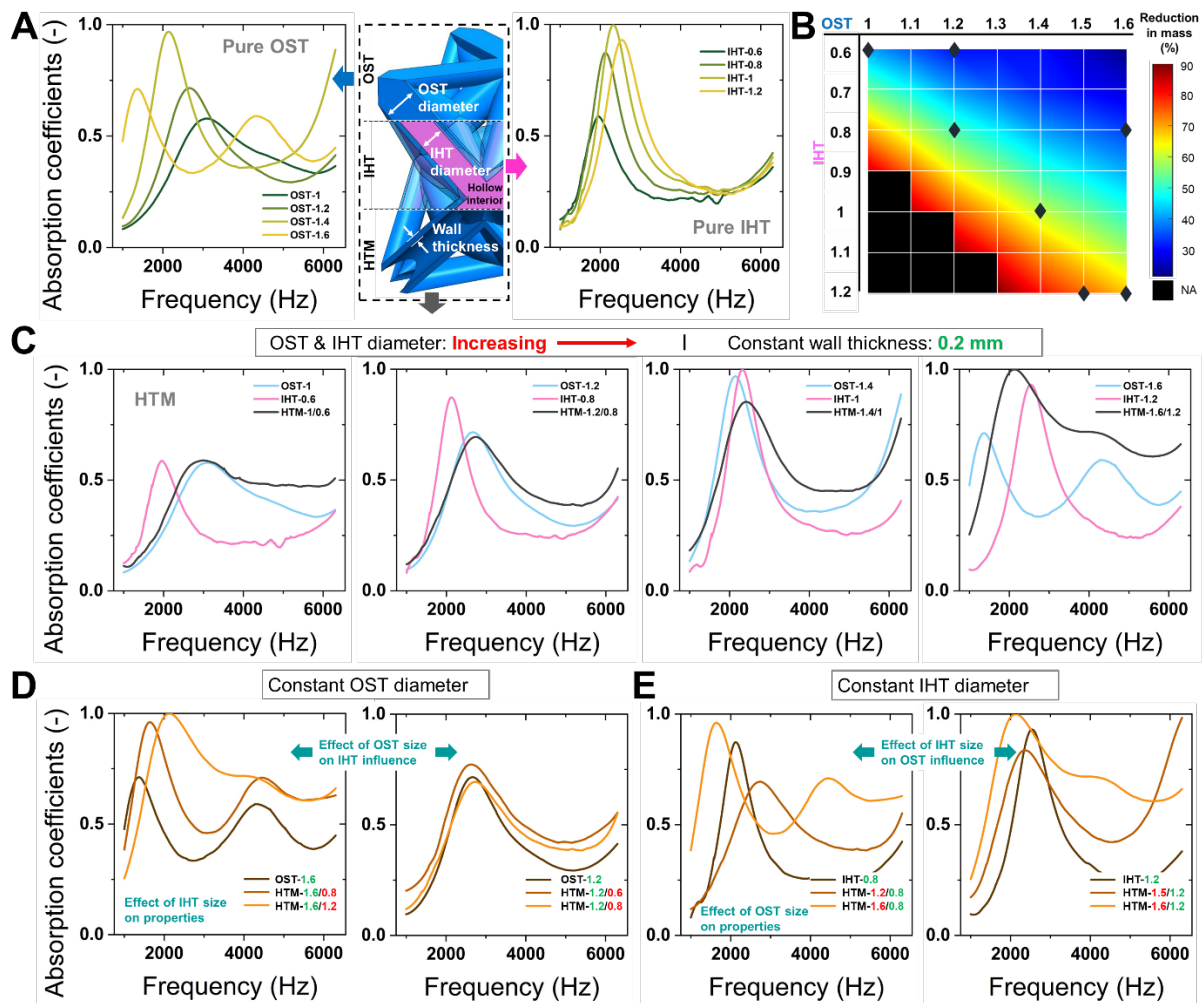

Figure 2: Summary of the OST, IHT, and HTM geometries under investigation and their experimentally measured sound absorption curves. (A) The experimentally measured sound absorption coefficient curves of pure OST and IHT structures, and a schematic of the HTM geometrical parameters. (B) An overall chart showing the OST and IHT strut diameters of the HTM expressed in millimetres. Values are denoted in the top row and left column, respectively. For each HTM, their respective mass reduction with the introduction of IHT is shown in the heat map with its corresponding colorbar. The HTMs adopted for experimental sound absorption studies are marked in the same figure. The experimentally measured sound absorption coefficient curves of (C) HTMs with a wall thickness of 0.2mm, and as compared

to their constituent phases; and HTMs, as compared when they have a (D) constant OST and (E) constant IHT diameter.

2.2 IHT absorption mechanisms

It is apparent that there is a complex size dependency (IHT and OST diameters) by the effective sound absorption of HTM. To understand the underlying mechanisms, we carry out analyses based on the individual acoustic impedances of each phase. There are two separate air phases within an HTM (**Figure 3A**). The two mechanisms associated with the sound absorption of HTM include: (i) the geometrical resonance associated with the IHT, and (ii) the Helmholtz resonance associated with the OST. We first give a separate breakdown of these mechanisms. The material properties used for the air in the following calculations are collated in the methods section.

Owing to its cubic symmetry, the unit cell of the HTM (hence including IHT and OST) can be further discretized into an irreducible zone, i.e., an eighth of a unit cell, for ease of numerical calculations. The eighth IHT unit cell consists of two separate, and complete tubular paths that sound waves can travel through (**Figure 3B**). For the torturous path, we first derive their associated tortuosity (χ). Based on computer-aided design calculations and curve-fitting, the relationship between the volume fraction of the lattice (Φ_v) and the strut diameter (d), expressed in millimetres, is given as:

$$\Phi_v = 0.436d - 0.16 \tag{1}$$

The volume of the lattice is then calculated by multiplying the volume of a cube with sides corresponding to the unit cell size L. A single complete tubular path is then based on a sixteenth of this unit, and its volume V_f can be expressed as:

$$V_f = (0.436d - 0.16)\frac{L^3}{16} \tag{2}$$

The effective distance (L_e) in which sound waves travel through the struts, as if the struts are stretched straight (**Figure 3Bii**), is based on the division of V_f by the strut's cross-sectional

area:

$$L_e = \frac{v_f}{\pi (d/2)^2} \tag{3}$$

Given χ to be the ratio between L_e and the actual material thickness,[31] i.e., the unit cell size L, χ for the IHP can thus be expressed as:

$$\chi = \left(\frac{D}{d}\right)^2 \left(\frac{4}{\pi}\right)(0.436d - 0.16) \tag{4}$$

The flow resistivity through a channel is associated with χ and is expressed as:[32]

$$\sigma = \frac{8\eta\chi}{\phi(d/2)^2} \tag{5}$$

ϕ refers to the porosity, per representative unit area on the surface. It is herein further normalized by dividing $\cos(\theta)$, where θ refers to the strut inclination angle, to account for the increased porosity with this geometry. θ is 45° and 55° for paths I and II, respectively. The characteristic viscous length through the hollow-strut is then given as:[33]

$$s = \sqrt{\frac{8\omega\rho_0\chi}{\sigma\phi}} \tag{6}$$

ω refers to the angular frequency given as $2\pi f$. Following these, the effective density can then be expressed as:[32, 34]

$$\rho = \rho_0 \left(1 + \frac{\sigma\phi}{i\omega\rho_0} G_c(s)\right) \tag{7}$$

G_c, as a function of s, is given as:

$$G_c(s) = -\frac{s}{4}\sqrt{-i}\frac{J_1(s\sqrt{-i})}{J_0(s\sqrt{-i})} \bigg/ \left[1 - \frac{2}{s\sqrt{-i}}\frac{J_1(s\sqrt{-i})}{J_0(s\sqrt{-i})}\right] \tag{8}$$

where i refers to the imaginary unit, J_0 and J_1 to the zeroth and first order Bessel functions, respectively.

The bulk modulus is in turn:[32, 34]

$$K = \frac{\gamma P_0}{[\gamma - (\gamma - 1)F(B^2\omega)]} \tag{9}$$

11

F, as a function of $B^2\omega$, is given as:

$$F(B^2\omega) = 1/\left[1 + \frac{\sigma\phi}{iB^2\omega\rho_0\chi}G_c(Bs)\right] \tag{10}$$

B^2 is the Prandtl number as given by $\eta/(\rho_0 v')$ where $v = \kappa/(\rho_0 c_p)$. Following the

derivation of ρ and K, the impedance at normal to the surface of an IHT is thus:[32]

$$Z_{IHT} = -i\frac{Z_c}{\phi}\cot(kL_e) \tag{11}$$

where $Z_c = \sqrt{K\rho}$ and $k = \omega\sqrt{\rho/K}$. The list of constants and their values used for

calculations in equations (5) – (11) are summarized in Table 1. Z_{IHT} is calculated for both

paths I and II. After which, they are then summed up in series to obtain the overall impedance

of the eighth of a unit cell. For its symmetry, this unit is representative of the entire unit cell.

The sound absorption coefficient, α, for a particular frequency, is then calculated as:

$$\alpha = \frac{4Re(Z_1/Z_0)}{[1 + Re(Z_1/Z_0)]^2 + Im(Z_1/Z_0)^2} \tag{12}$$

$$Z_0 = \rho_0 c_0 \tag{13}$$

The absorption curve is then obtained via calculation through the entire range of frequency.

Good agreements between the numerical calculations and experiments have been achieved.

Plots are illustrated in **Figure S2**, Supporting Information.

2.3 OST absorption mechanisms

Similarly, we work on an eighth of the unit OST air phase as shown in **Figure 3Ci**.

The OST can be discretized into an arrangement of alternating small pores and large cavities

along the incident sound wave direction (**Figure 3Cii**). Such a structure is akin to a series

connection of Helmholtz resonators.[16] The overall sound absorption of such a structure is

hence primarily dependent on four geometrical parameters, namely the pore diameter (d_p), the

surface porosity (ε), pore thickness (t) and cavity depth (D) in the direction of the incident

wave, and secondarily, the number of unit cells through-thickness (N). Details on obtaining the geometrical parameters are shown in **Figure S3**, Supporting Information. To obtain the acoustic impedance of the multi-layered structure, we perform a transfer impedance series addition of all the layers, starting from the bottom to the top.

There are two types of acoustic impedances associated with the multi-layered Helmholtz resonator – that from the small pores (also known as perforations), and that from the cavity immediately following (**Figure 3Cii**). Consisting of both the impedance of the perforation and the cavity, the impedance of any n^{th} layer (Z_n), where the subscript n refers to that particular layer, equals to the linear sum of the impedance of the perforation (Z_P) and its immediate cavity (Z_{Cn}).

$$Z_n = Z_P + Z_{Cn} \qquad (14)$$

The impedance of the perforation is solely geometry dependent on (d_p, t, ε), and is inter-layer independent. It is expressed as:[16]

$$Z_P = \frac{32\eta t}{d_p{}^2 \varepsilon}\left(\sqrt{1 + \frac{k^2}{32}} + 2\beta R_s\right) + i\frac{\omega\rho_0 t}{\varepsilon}\left(1 + \left(9 + \frac{k^2}{2}\right)^{-\frac{1}{2}} + \frac{\delta}{t}\right) \qquad (15)$$

k refers to the perforate constant as given by $k = d_p\sqrt{\rho_0\omega/4\eta}$. $2\beta R_s$ is the resistance end correction factor and $R_s = 1/2\sqrt{2\eta\rho_0\omega}$ and β = 4.[35] $\delta = 0.68d_p(1 - 1.14\sqrt{\varepsilon})$ is the reactance end correction term as adapted from Allard *et al.* and corrected for a triangular pore geometry.[32]

The cavity impedance is in turn dependent on the Z_n of the previous layer. Since the OST structure ends with a cavity (**Figure 3Cii**), Z_{Cn} of the bottom layer hence equals to solely the impedance of the cavity's geometry. For a structure with N number of layers, starting from N to 1, the bottom layer cavity impedance can be represented as:

$$Z_{CN} = -iZ_0 \cot\left(D\frac{\omega}{c_0}\right) \qquad (16)$$

13

The subsequent layer, $Z_{C(N-1)}$, is in turn dependent on Z_N and can be expressed as:[36]

$$Z_{Cn} = Z_0 \frac{Z_{n+1} \cos\left(D\frac{\omega}{c_0}\right) + iZ_0 \sin\left(D\frac{\omega}{c_0}\right)}{Z_0 \cos\left(D\frac{\omega}{c_0}\right) + iZ_{n+1} \sin\left(D\frac{\omega}{c_0}\right)} \tag{17}$$

Equations (14) – (17) sum up the expressions for calculating the impedance of each layer.
Given the structural complexity of the OST, each layer needs to be further broken down for a
clear illustration of the connectivity. The inverse of the OST, the air phase, is shown in
Figure 3Cii. It is to note that the inverse of the OST is essentially a close-pack arrangement
of a rhombic dodecahedron (RD) like structure. Again, discretizing into an eighth of a unit
column, two types of different layers are observed for the OST:

- Type-A: Parallel arrangement of two 1/8 RD

- Type-B: 1/4 of the RD

Despite the varying layers, given that they consist of the same RD unit motif, the geometrical
parameters of concern (for Z_P and Z_{Cn}) relevant to calculations are still the same throughout.
As such, parallel transfer impedance calculations from a Type-B to Type-A layer then
simplify into:

$$Z_n = \frac{A_2}{\frac{A_1}{Z_{n+1}} + \frac{A_1}{Z_{n+1}}} \tag{18}$$

A_1 and A_2 refer to the planar area proportion of the air phases and they essentially simplify
into their RD volume ratio. The transfer impedance from a Type-A to Type-B layer then
follows the series transfer. As can be seen in **Figure 3Ciii**, there are a total of 6 layers, each
consisting of a cavity and perforation layer, in the OST. The effective impedance of the OST
(Z_{OST}) is then given by Z_1, which is derived iteratively after the transfer calculations from Z_6,
Z_5 … to Z_1 completes. Using Z_{OST}, the sound absorption coefficients are then calculated in a
similar way to that in equation (12). Good agreements between the numerical calculations

and experiments have also been achieved as summarized in **Figure S4**, Supporting
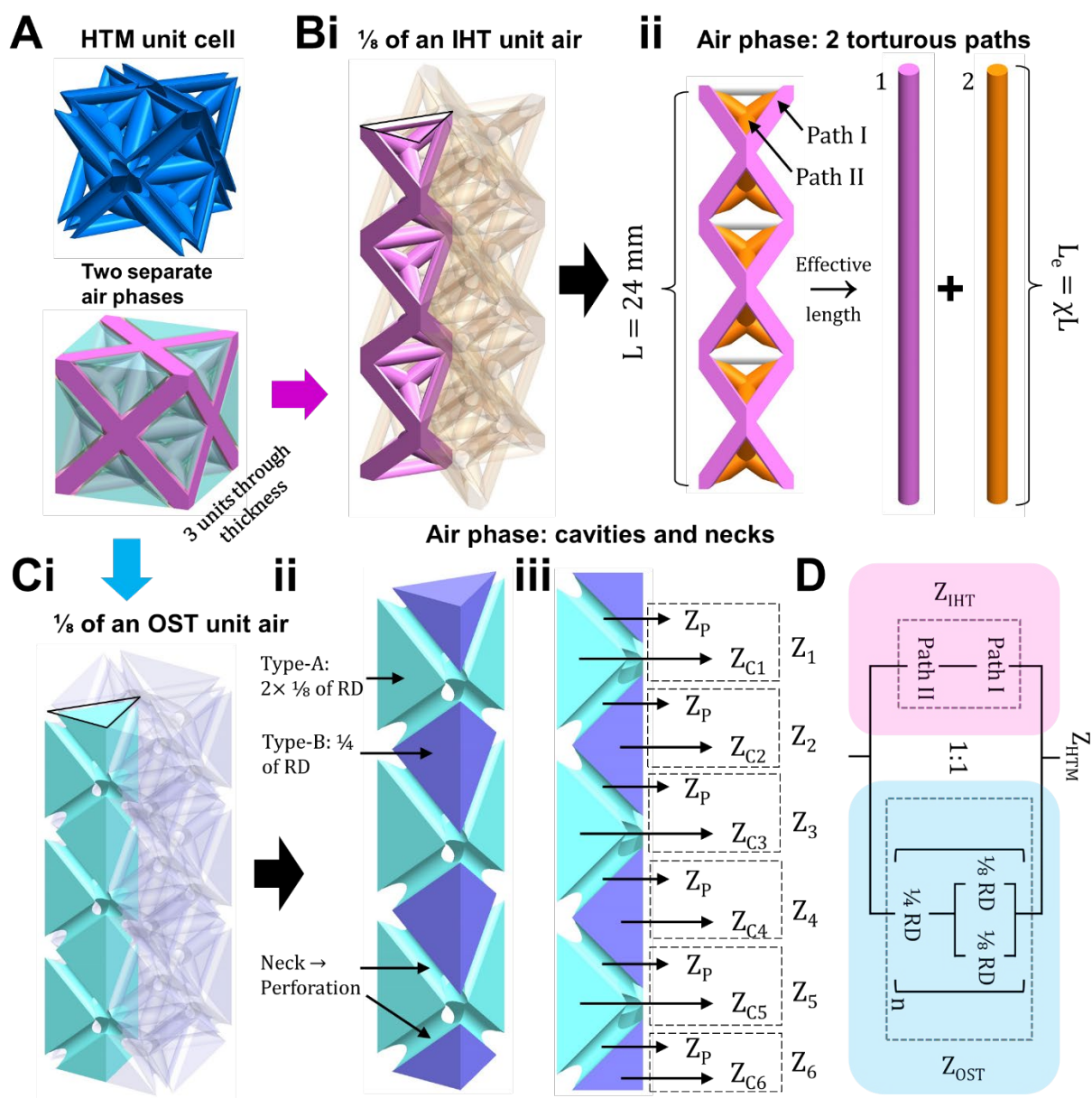
Information.

Figure 3: Sound dissipation mechanism of the HTM. (A) Illustration of an HTM unit cell and

the two separate air phases it contains. (Bi) Illustration of an eighth of an IHT unit air,

repeated three times through-thickness; (ii) the two torturous paths through the unit. (Ci)

Illustration of an eighth of an OST unit air, repeated three times through thickness; (ii) the

Type-A and B layers, and the neck perforation regions; (iii) the acoustic impedances for the

cavity and perforation of each layer. (D) Illustration of the overall acoustic impedance circuit.

2.4 HTM absorption mechanism

Having the mechanisms of their individual forms affirmed, a summation will be required to obtain the overall HTM acoustic impedance and hence the sound absorption curve. As can be seen, within the HTM, the IHT and OST are separated by a solid wall and no lateral airflow is possible (**Figure 3A**). This implies that the parallel addition rule would be the appropriate summation in such a scenario.[17] With their porosities already being taken into account of, Z_{IHT} and Z_{OST} are then summed up in parallel by the same unit cell surface area (A'), and thus in a ratio of 1:1, as shown in equation (19). The overall impedance circuit map is shown in **Figure 3D**. It is to note that the total area is also given by A' since the two phases are superimposed onto each other.

$$Z_{HTM} = \frac{A'}{\frac{A'}{Z_{IHT}} + \frac{A'}{Z_{OST}}} = \frac{1}{\frac{1}{Z_{IHT}} + \frac{1}{Z_{OST}}} \tag{19}$$

Good agreements between numerical calculations and experiments have also been observed for the HTM (**Figure S5**, Supporting Information). Therefore, we can draw information from their acoustic impedances with confidence to obtain an understanding of the structural and contribution relationships. The acoustic impedance (denoted as Z) consists of two parts, the air resistance based on the real part (Re(Z)), and the air mass reactance, based on the imaginary (Im(Z)). Physically speaking, the resistance describes the energy loss in the structure whilst the reactance determines the frequency where the highest dissipation occurs. To achieve the highest sound energy dissipation, or total sound absorption, i.e., $\alpha = 1$, it is noted from equation (12) that Re(Z) and Im(Z) should be ideally 1 and 0, respectively. For such a scenario, the impedance is said to be critically coupled. The resistance and reactance curves of the OST, IHT, and HTMs, extracted based on their final Z values, are plotted in **Figure 4A,B**. Similar to the trend observed in **Figure 2B** for their absorption coefficients, the

frequencies with the highest absorption (resonance peaks) correspond to that with Re(Z) and Im(Z) simultaneously close to ideal values.

We then proceed to use two contrasting cases, HTM-1.6/1.2 and HTM 1/0.6, to illustrate the combined absorption mechanism. Z_{OST} and Z_{IHT} are plotted alongside their respective Z_{HTM}. Overall, it is found that the resulting Re(Z_{HTM}) curve corresponds to the superimposed portions of the Re(Z_{OST}) and Re(Z_{IHT}) curves where their values are closer to 1. The Im(Z_{HTM}) curve then varies between Im(Z_{OST}) and Im(Z_{IHT}) if they are close to each other, while it follows the curve closer to 0 if Im(Z_{OST}) and Im(Z_{IHT}) differ significantly. We turn to a specific example using HTM-1.6/1.2 for illustrations (**Figure 4Bi**). For Re(Z), in the region of around 1000 – 4500 Hz, the resistance of IHT-1.2 is much closer to 1 than OST-1.6. The Re(Z_{HTM}) curve therefore follows closely to that of Re(Z_{IHT}), bypassing the anti-contributions from Re(Z_{OST}). However, beyond around 4500 Hz, Re(Z_{IHT}) increases sharply and Re(Z_{OST}) in turn becomes much closer to 1. A crossover point, from following Re(Z_{IHT}), to Re(Z_{OST}), hence exists. For Im(Z), given that Im(Z_{OST}) and Im(Z_{IHT}) are rather close to each other, the resulting Im(Z_{HTM}) curve hence lies somewhere in between the two. A schematic illustration of the physical phenomenon is shown in a proposed dissipation band diagram in **Figure 4Bii**. Dissipations of the OST and IHT are represented by their bar charts and a higher dissipation is denoted by a thicker bar. Depending on the frequency band, dissipation occurs most rapidly at either the OST or IHT and points of crossovers(s) exist. There are comparable contributions across the entire frequency range by both phases and Z_{HTM} is hence brought closer to being ideal. Therefore, HTM-1.6/1.2 leverages the advantages of both of its constituents and the combination is said to be compatible. However, contrasting observations have been made for HTM-1/0.6. Throughout almost the entire frequency range, Re(Z_{IHT}) and Im(Z_{IHT}) are observed to deviate significantly further from 1 and 0, respectively, as compared to Re(Z_{OST}) and Im(Z_{OST}) (**Figure 4Ci**). Re(Z_{HTM}) hence

follows closely to $\mathrm{Re(Z_{OST})}$ owing to its lower resistance whilst $\mathrm{Im(Z_{HTM})}$ follows closely to $\mathrm{Im(Z_{OST})}$ since $\mathrm{Im(Z_{IHT})}$ lies to be significantly further. Dissipation in IHT-0.6 is bypassed almost entirely and it provides minimal contributions to moving the curves closer to ideal values (**Figure 4Cii**). This is consistent with the observations in **Figure 2C** where the absorption curve of HTM-1/0.6 follows closely to that of OST-1. In addition, the resistance and reactance of OST-1 and IHT-0.6 also deviate significantly further away from ideal values as compared to their counterparts in HTM-1.6/1.2. On top of that, HTM-1.6/1.2 leverages the advantages of both of its constituents with an almost equal contribution of both. The superior sound absorption of HTM-1.6/1.2 as compared to HTM-1/0.6 therefore attributes to two factors: better (i) dissipation capabilities and the (ii) compatibility of its constituent structures.

We hence conclude that the HTM absorption mechanism is based on the superimposed critically coupled impedance paths, at different frequency bands, of the two phases. The same observations are made for the other HTMs and their respective impedance curves are plotted in **Figure S6**, Supporting Information. As can be seen, the overall mechanism has a complex inter-dependency on both the IHT and OST diameters and it is also frequency dependent. A (non)linear measure of their degrees of contributions to the overall absorption would hence not be applicable herein. Following this, an overall observation, shown in **Figure 4C**, can be made from the trends. Judging from the analyses, it can be said that the OST is more dominant given its $\mathrm{Re(Z)}$ and $\mathrm{Im(Z)}$ values which are closer to ideal. The most synergistic contribution from both phases occurs with OST-1.6. When the OST sizes are small, IHTs contribute little and the HTM absorption curves generally follow that of the OST (**Figure 2C**). In the middle, moderate contributions from the IHT are observed for OST-1.4 and OST-1.5. It can be seen that there is a concept of strut diameter compatibility to achieve the highest absorption. For our HTMs, it is determined that

compatibility increases with simultaneously thicker OST and IHT struts. Otherwise, customizable absorption curves and weight reductions (**Figure 2B**) can be achieved with moderately compatible and incompatible HTM geometries, respectively. The mechanism presented in **Figure 4** also serves as a design guideline for HTMs.
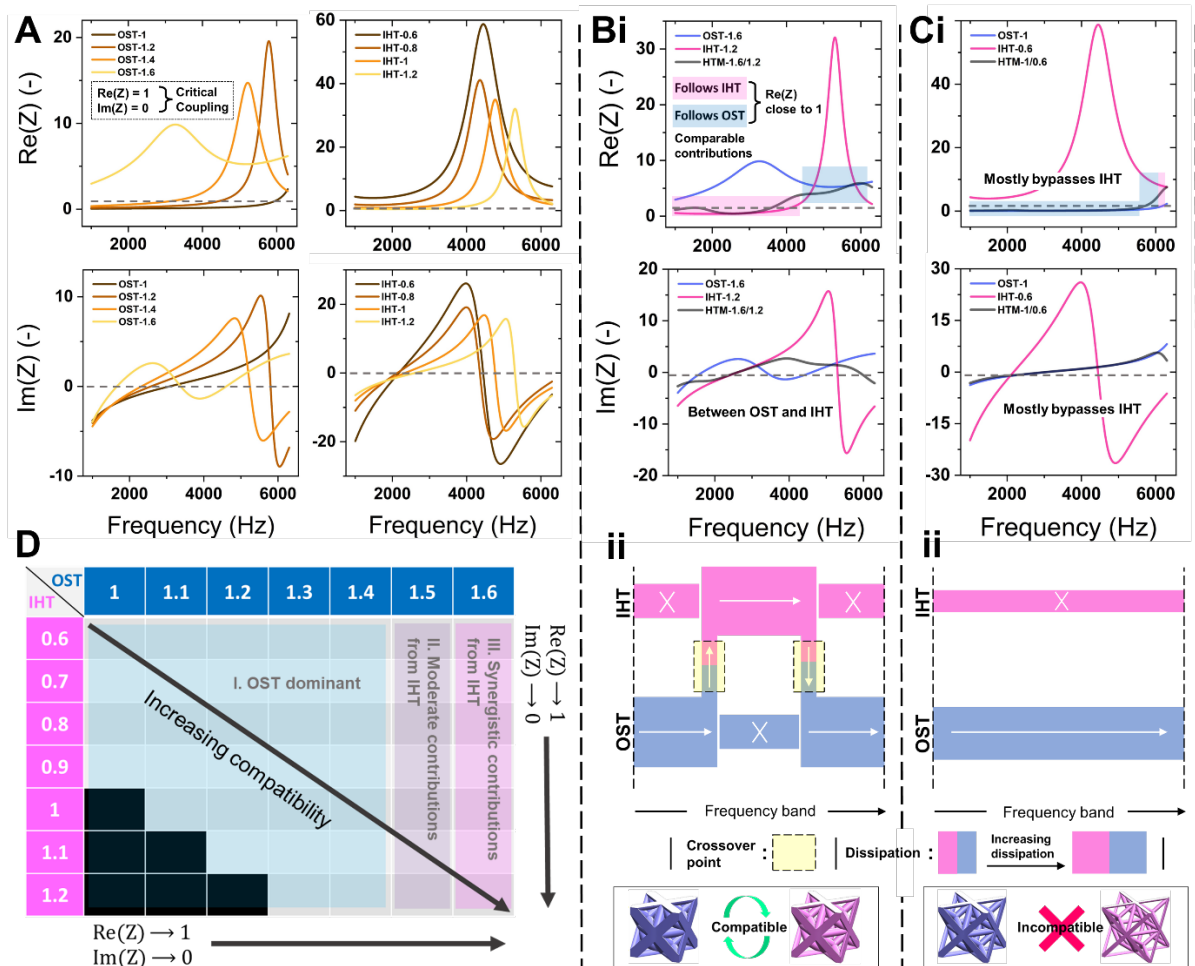

Figure 4: The effective acoustic impedance of the HTM and structural compatibility. The resistance and (A) The numerically calculated Re(Z) and Im(Z) curves for the OSTs and IHTs, across a range of diameters. (Bi) The Re(Z) and Im(Z) curves of HTM-1.6/1.2 and constituents and (ii) a frequency band schematic for the case of compatible OST and IHT geometries. (Ci) The Re(Z) and Im(Z) curves of HTM-1/0.6 and constituents and (ii) a frequency band schematic for the case of incompatible OST and IHT geometries. (D) An

overall summary of the compatibility of different OST and IHT phases in their respective HTMs.

2.5 Compressive properties

Complementary to sound absorption properties, the compressive energy absorption characteristics of the HTMs are next investigated. There are two primary parameters which characterize the HTM: the OST radius (r), and the wall thickness (w) to the OST radius (w/r) ratio. The HTMs and OSTs (w/r = 1) selected for compression tests are shown in **Figure 5A**. Experimental findings reveal a high dependency of specific energy absorption (SEA) on both r and w/r. The stress-strain curves of OST and HTMs measured under quasi-static compression tests are shown in **Figure 5B**. OSTs display high compression strengths followed by immediate post-compression valleys characterized by a high negative stress-strain gradient. Their behaviours are characteristic of highly stretch-dominated truss microlattices.[2] For OST-1.6, abrupt failure occurs at an early onset with the loss of load-bearing capabilities around -0.3 strain. Distinctly different from the OSTs, HTMs display a highly reduced post-compression valley and they present stable plateau stress deformation behaviors. This reduction is additionally more prominent with a lower w/r ratio. Specific energy absorption (SEA), calculated via the work done up to densification, is plotted onto the same figure in **Figure 5A**. As shown from the plot, a lower r gives higher SEA values. Additionally, an optimal SEA exists at a moderate w/r ratio, e.g., such as 0.5 in this work. In fact, HTM-1.6/0.8 displays an improved SEA by up to around 50% from HTM-1.6.

Observations leading up to these compressive behaviours are shown in the captured deformation sequences in **Figure 5C**. As evident from **Figure 5Ci**, the main deformation mechanism of the OSTs lies with the material failure, either compression, shear or tension, of the struts in the stretch-dominated configuration. An abrupt brittle rupture of the entire lattice,

from a low strain of -0.1, is hence observed for the OSTs. This results in the early loss of

load-bearing capabilities of OSTs as observed in **Figure 5B**. For the HTMs, their mode of

deformation is in turn more structural-based as evident from the cell wall

folding/bending/tearing and sequential macroscopic shear bands (**Figure 5Cii**).[37] Different

from OSTs, there is no presence of abrupt rupture and the HTMs are also observed to be well

intact at -0.1 strain. This hence results in the HTMs to deform with a characteristic plateau

stress and densification zone, similar to ductile microlattices.[38-39] The combination of a long

plateau stress region, along with the reduced mass, results in improved SEA for the HTMs.

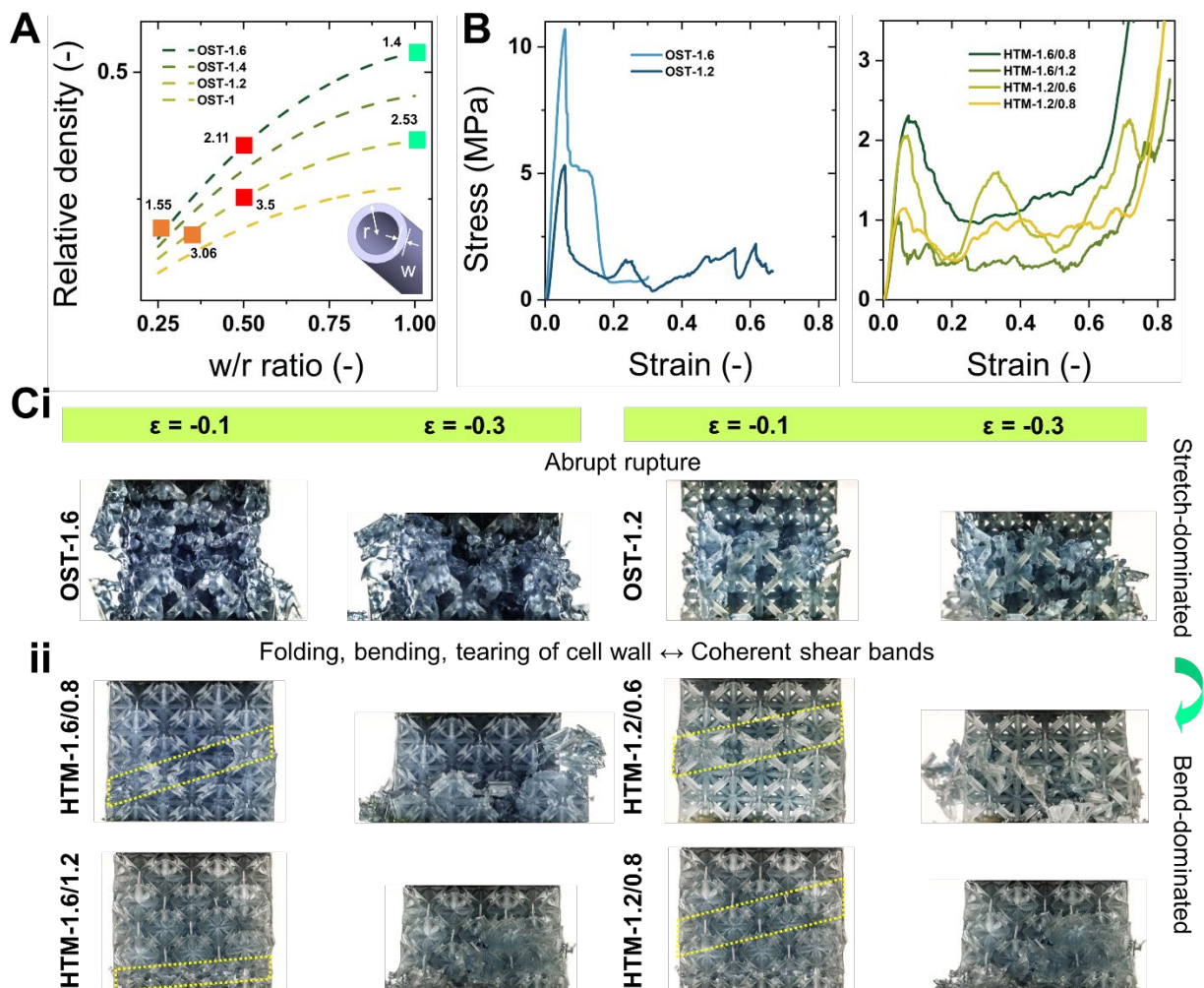Overall, the concept of "less is more", is also illustrated for energy absorption.

Figure 5: Compressive properties and specific energy absorption of selected HTMs and

OSTs. An overview of the mechanical properties. (A) An overall plot of the relative density,

with respect to the w/r ratio, for HTM samples with different OST diameters. The samples chosen for experimental compression tests are marked out on the same plot. Their measured SEA values are indicated on the same plot. (B) The representative compressive stress-strain curves of the OST and HTM samples. (C) The captured digital images of the deformation sequence of the samples.

3. Further discussion

Traditionally, the sound absorption mechanisms of microlattices are based primarily on resonance or flow resistance. This limits the bandwidth and coefficients of the absorption curves. Despite being capable of achieving near unity coefficients, resonance-based microlattices generally display absorption peaks characterized by a narrow bandwidth.[15, 18] In turn, microlattices based on flow resistance display low absorption coefficients despite having a wider bandwidth.[24-25] All in all, across a wide bandwidth, microlattices based on a homogeneous unit cell generally tend to display low averaged absorption coefficients (**Figure 6**).[15, 18, 24, 40] For microlattices based on either mechanism, to improve broadband sound absorption performances, efforts have been placed on additive means, e.g. introducing heterogeneity to the neighbouring cells, or functionally-graded successive cells. However, these types of non-uniform structures are generally size-limited. A unit absorption area (or unit cell) of a heterogeneous microlattice would then be extended to consist of all of its heterogeneous units, e.g. four cells,[17] ten meta-units,[41] three orders of hierarchy,[42] etc. Functionally-graded microlattices are in turn extended in the thickness direction with cells of varying sizes.[21-22, 40] The abovementioned techniques in improving sound absorption performance does not take into considerations of the volume-space constraint (**Figure 6**).

Herein, on the basis of the truss microlattice, as opposed to additive methods, we improve its sound absorption performance by a conceptually novel methodology, an *in-situ*

subtraction of its materials. This reduction is carried out by hollowing out the struts of the truss architecture, such that the microlattice consists of two separate continuous air domains bounded by the outer-solid and the inner-hollow phases. This then constitutes the HTM to display dual dissipation mechanisms, based on the (i) Helmholtz resonance from its complex truss interconnectivity, and the (ii) geometrical resonance of its hollow interior. Such a dual-functioning mechanism had not been previously reported. At a compatible set (inner and outer) of strut diameter, e.g., HTM-1.6/1.2, drastic improvements in the absorption coefficients have been observed. Being subtractively enhanced, our HTM hence does not suffer from increased volume and mass. In fact, as compared, our HTM is much thinner at a thickness of 24 mm whereas mainstream samples are usually thicker than 30 mm.[15, 17-18, 21-22, 40] The average coefficient of HTM-1.6/1.2 at 0.72 compares favourably with that of the reported values of various (homogeneous, heterogeneous, functional graded) microlattices[15, 17-18, 21-22, 40] and foams[24] that are measured in the similar frequency range. With a lower thickness of 24 mm, HTM-1.6/1.2 then compares superior in terms of a higher coefficient-to-thickness ratio (**Figure 6**). Meanwhile, improved SEA, across a range of HTM geometries, is also achieved given the improved compressive toughness observed. All of these achievements are remarkable considering that the gains are achieved via a 68% reduction in the mass of the material. The HTM concept is also universal for any type of truss-lattice architecture. Nonetheless, different sound dissipation mechanisms or absorption properties would be expected from different structures. For instance, the existence of the Helmholtz resonance dissipation mechanism depends on the interconnectivity of the lattice structures, i.e., whether a pore-and-cavity morphology exists in the OST (**Figure 3C**). Where applicable, the strut arrangements influence the number of necks and cavities, their effective number of resonating cells through the structure (N), the perforation geometrical parameters (d_P, t, D), and the surface porosity (ε).[15] For the IHT, the tortuosity (χ) is directly influenced by the

complexity of the architecture while the surface porosity (ϕ) is influenced by both this complexity and the strut diameter (d) (**Figure 3B**). Therefore, different lattice architectures may result in vastly different parameters related to the OST and IHT dissipation mechanisms and modifications to the acoustic impedance calculations might be needed. The HTM class of material can also be fabricated using advanced hybrid additive manufacturing techniques, such as the deposition-etching class of techniques.[43-44] In fact, these allow the extension of the design space, such as smaller struts or thinner cell walls, beyond what is presented in this work. With the potential shown in this work, we envisage that new lattice designs and extended geometrical allowances may result in metamaterials with further unprecedented acoustics properties.
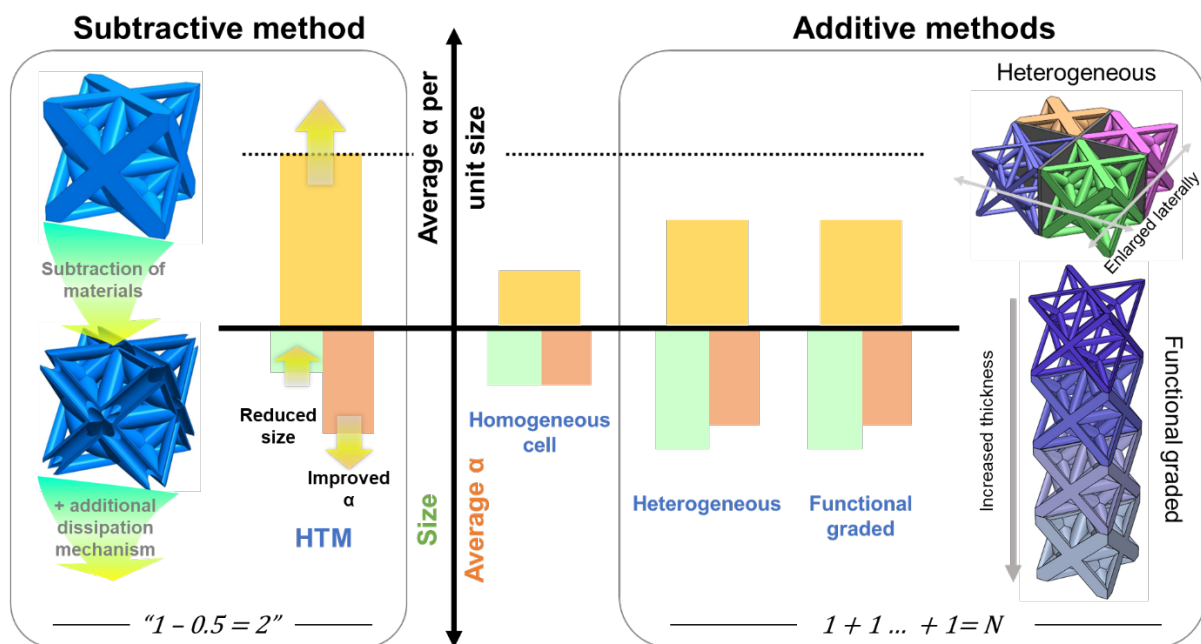

Figure 6: A schematic illustration of the overall sound absorption performance of the HTM as compared to microlattices reported in literature. The figure also illustrates the subtractive method that we have used herein (that derived the HTM) as opposed to additive methods reported in the literature to improve sound absorption performances. References used to aid in the comparison are as follows: homogeneous, [15, 18, 24, 40] heterogeneous,[17] functional graded.[21-22, 40].

4. Conclusion

In summary, we have proposed and experimentally validated, via additive manufacturing, a novel concept of hollow-truss metamaterial (HTM) for effective broadband and high sound absorption. As opposed to their solid-truss counterparts, the HTMs harness an additional sound dissipation mechanism, from the geometrical resonance of their inner-hollow phase, apart from the innate Helmholtz resonance from their out-solid phase. Through acoustic impedance calculations, we have proposed a numerical model for analysing the acoustic impedances of the HTM. A new dissipation mechanism for the HTM, based on the superimposed path of the critically coupled resistance and mass reactance of the two phases across different frequency bands, is proposed. In general, if the resistances of the two phases are in close proximity to each other, and each has its regions that are close to the ideal resistance of 1, the resulting resistance of the HTM would be a superimposed curve based on the regions close to the ideal value. If one is dominantly further from 1 than the other, the one that is far would be bypassed. Similar deductions are made for mass reactance too. The acoustic impedance, and thus the absorption coefficients, are hence highly dependent on the diameters of the outer-solid and inner-hollow struts. The HTMs display superior and/or customizable sound absorption coefficients as compared to their constituents.

In this work, the best combination is based on an HTM with an outer diameter of 1.6 mm and an inner diameter of 1.2 mm. The average absorption coefficient of this structure, across a broad range of frequencies from 1000 – 6300 Hz, measures to be 51.1 and 84.4% higher than its pure solid and hollow strut constituents, respectively. The effective bandwidth is also drastically improved, where 90.4% of its absorption coefficients are above a high value of 0.6, as compared to 10.9% and 17.9% of its formerly mentioned constituents. Complementary to sound absorption, compressive mechanical properties also reveal improved SEA, up to an increase of 50%, from the enhanced plateau deformation behaviour

of the hollow struts. Remarkably, all these improvements are achieved via a large 68%

reduction of mass, as opposed to a gain. These fully illustrate the concept of "less is more",

where with less materials, we achieve a gain in better properties.

5. Experimental section

Numerical calculations and design: Standard tessellation language (.stl) files used for 3D

printing were modelled using SolidWorks. For all of the experiments, a cubic unit cell with a

side of 8 mm was adopted. For sound absorption measurements, the unit cell is repeated

3×3×3 such that the overall structure consists of 27 unit cells with a thickness of 24 mm in

the direction of the sound wave. Owing to the tubular geometry of the impedance tube, slight

extrusion cuts were made to the edges of the overall structure. Compression samples are in

turn based on the overall cubic structure with 3×3×3 unit cell repetitions. Both OST and

HTM samples are designed and 3D printed as they would appear to be. However, since the

pure IHT is based on hollow tubes, the IHT is 3D printed based on the inverse of the hollow

truss structure instead. All of the abovementioned 3D printing designs and some

representative as-printed samples are illustrated in **Figure S7,8**, Supporting Information.

Numerical calculations of the acoustic impedance and absorption coefficient curve were

coded using the MATLAB programming language. The material constants for air used for

equations (1) – (16) are collated in Table 1.

Table 1: The list of constants and expressions for air, at standard temperature and pressure, used in the numerical calculations.

Constant	Expression	Value [Units]
Speed of sound	c	343 [m s^{-1}]
Density	ρ_0	1.21 [kg m^{-3}]
Dynamic viscosity	η	1.846×10^{-5} [Pa·s]
Pressure	P_0	1.01×10^5 [Pa]
Thermal conductivity	κ	2.614×10^{-2} [W (mK)$^{-1}$]
Heat capacity	c_p	718 [J (kgK)$^{-1}$]
Ratio of specific heat	γ	1.4 [-]

3D printing: The designed structures are 3D printed using the digital light processing technique (DLP) with the Asiga Max X27 DLP (Asiga, Australia). The material in use is Nova Stan, a 405 nm wavelength curable photosensitive resin, from Nova3D, China. Main DLP printing parameters include a light intensity of 5 mW cm^{-2}, layer thickness of 100 μm, and an exposure time of 1.5 s for each layer. After printing, the parts are thoroughly washed using isopropyl alcohol for around 20 minutes to remove the excess resin. After allowing to fully dry, the parts are then post-cured in an ultraviolet chamber, Asiga Flash, for 1 h to allow full curing. The parts are then used for both sound absorption and compression tests as-prepared after this step.

Sound absorption measurements: Sound absorption measurements were carried out using the BSWA SW477 (BSWA Tech, China) impedance tube in accordance with ISO 10534-2 standards. This tube has a diameter of 30 mm which corresponds to our frequency range of interest from 1000 to 6300 Hz. Sound absorption coefficient curves were reported based on the average of three readings.

Compression tests: Quasi-static compression tests were carried out at a strain rate of 0.001 s^{-1} using the Shimadzu AG25-TB (Shimadzu Corporation, Japan) universal testing machine. The contact surfaces of the samples and the compression platens were greased to reduce friction. A digital camera was used to capture the deformation sequences of the samples.

Supporting Information

Supporting Information is available from the Wiley Online Library or from the author.

References

[1]   M. C. Fernandes, J. Aizenberg, J. C. Weaver, K. Bertoldi, *Nat. Mater.* **2021**, 20, 237.

[2]   A. Mao, N. Zhao, Y. Liang, H. Bai, *Adv. Mater.* **2021**, 2007348.

[3]   T. Tancogne‑Dejean, M. Diamantopoulou, M. B. Gorji, C. Bonatti, D. Mohr, *Adv. Mater.* **2018**, 30, 1803334.

[4]   J. Bauer, J. A. Kraus, C. Crook, J. J. Rimoli, L. Valdevit, *Adv. Mater.* **2021**, 2005647.

[5]   J. Mueller, J. R. Raney, K. Shea, J. A. Lewis, *Adv. Mater.* **2018**, 30, 1705001.

[6]   X. Su, X. Li, C. Y. A. Ong, T. S. Herng, Y. Wang, E. Peng, J. Ding, *Adv. Sci.* **2019**, 6, 1801670.

[7]   T. Chen, M. Pauly, P. M. Reis, *Nature* **2021**, 589, 386.

[8]   J. Mueller, J. A. Lewis, K. Bertoldi, *Adv. Funct. Mater.* **2022**, 32, 2105128.

[9]   H. M. Kolken, S. Janbaz, S. M. Leeflang, K. Lietaert, H. H. Weinans, A. A. Zadpoor, *Mater. Horiz.* **2018**, 5, 28.

[10]   C. Jia, L. Li, Y. Liu, B. Fang, H. Ding, J. Song, Y. Liu, K. Xiang, S. Lin, Z. Li, *Nat. Commun.* **2020**, 11, 1.

[11]   M. Yang, P. Sheng, *Annu. Rev. Mater. Res.* **2017**, 47, 83.

[12]   N. Gao, J. Wu, K. Lu, H. Zhong, *Mech. Syst. Signal Process.* **2021**, 154, 107504.

[13]   N. Gao, Z. Zhang, J. Deng, X. Guo, B. Cheng, H. Hou, *Adv. Mater. Technol.* **2022**, 2100698.

[14]   X. Zhang, Y. Wang, B. Ding, X. Li, *Small* **2020**, 16, 1902842.

[15]   X. Li, X. Yu, J. W. Chua, H. P. Lee, J. Ding, W. Zhai, *Small* **2021**, 2100336.

[16]   D.-Y. Maa, *J. Acoust. Soc. Am.* **1998**, 104, 2861.

[17]   X. Li, X. Yu, W. Zhai, *Adv. Mater.* **2021**, 2104552.

[18]   T. G. Zieliński, K. C. Opiela, P. Pawłowski, N. Dauchez, T. Boutin, J. Kennedy, D. Trimble, H. Rice, B. Van Damme, G. Hannema, *Addit. Manuf.* **2020**, 36, 101564.

[19]   Z. Li, W. Zhai, X. Li, X. Yu, Z. Guo, Z. Wang, *Virtual Phys. Prototyp.* **2022**.

[20]   W. Zhai, X. Yu, X. Song, L. Y. L. Ang, F. Cui, H. P. Lee, T. Li, *Mater. Des.* **2018**, 137, 108.

[21]   J. Boulvert, T. Cavalieri, J. Costa-Baptista, L. Schwan, V. Romero-García, G. Gabard, E. R. Fotsing, A. Ross, J. Mardjono, J.-P. Groby, *J. Appl. Phys.* **2019**, 126, 175101.

[22]   J. Boulvert, J. Costa-Baptista, T. Cavalieri, M. Perna, E. R. Fotsing, V. Romero-García, G. Gabard, A. Ross, J. Mardjono, J.-P. Groby, *Appl. Acoust.* **2020**, 164, 107244.

[23]   X. Cai, J. Yang, G. Hu, T. Lu, *J. Acoust. Soc. Am.* **2018**, 144, EL138.

[24]   X. Yu, Z. Lu, W. Zhai, *Acta Mater.* **2021**, 206, 116666.

[25]   W. Yang, J. An, C. K. Chua, K. Zhou, *Virtual Phys. Prototyp* **2020**, 15, 242.

[26]   S. Deshmukh, H. Ronge, S. Ramamoorthy, *Mater. Des.* **2019**, 175, 107830.

[27]   M. Yang, S. Chen, C. Fu, P. Sheng, *Mater. Horiz.* **2017**, 4, 673.

[28]   G. Y. Song, Q. Cheng, B. Huang, H. Y. Dong, T. J. Cui, *Appl. Phys. Lett.* **2016**, 109, 131901.

[29]   J. Du, Y. Luo, X. Zhao, X. Sun, Y. Song, X. Hu, *Sci. Rep.* **2021**, 11, 1.

[30]   W. Huang, L. Schwan, V. Romero-García, J.-M. Génevaux, J.-P. Groby, *Sci. Rep.* **2019**, 9, 1.

[31]   J. G. Fourie, J. P. Du Plessis, *Chem. Eng. Sci.* **2002**, 57, 2781.

[32]   J. Allard, N. Atalla, *Propagation of sound in porous media: modelling sound absorbing materials 2e*, John Wiley & Sons, **2009**.

[33]   Y. Champoux, J. F. Allard, *J. Appl. Phys.* **1991**, 70, 1975.

[34]   M. R. Stinson, *J. Acoust. Soc. Am.* **1991**, 89, 550.

[35]   S. Allam, M. Åbom, *Journal of vibration and acoustics* **2011**, 133.

[36]   Y. Tang, S. Ren, H. Meng, F. Xin, L. Huang, T. Chen, C. Zhang, T. J. Lu, *Sci. Rep.* **2017**, 7, 43340.

[37]   J. Noronha, M. Qian, M. Leary, E. Kyriakou, M. Brandt, *Curr. Opin. Solid State Mater. Sci.* **2021**, 25, 100940.

[38]   L. Zhang, S. Feih, S. Daynes, S. Chang, M. Y. Wang, J. Wei, W. F. Lu, *Addit. Manuf.* **2018**, 23, 505.

[39]   X. Li, Y. H. Tan, H. J. Willy, P. Wang, W. Lu, M. Cagirici, C. Y. A. Ong, T. S. Herng, J. Wei, J. Ding, *Mater. Des.* **2019**, 178, 107881.

[40]   X. Zhang, Z. Qu, D. Tian, Y. Fang, *Appl. Acoust.* **2019**, 151, 22.

[41]   Z. Ren, Y. Cheng, M. Chen, X. Yuan, D. Fang, *Mater. Des.* **2022**, 215, 110462.

[42]   Z. Wang, Z. Guo, Z. Li, K. Zeng, *Appl. Phys. Lett.* **2021**, 119, 171903.

[43]   X. Zheng, W. Smith, J. Jackson, B. Moran, H. Cui, D. Chen, J. Ye, N. Fang, N. Rodriguez, T. Weisgraber, *Nat. Mater.* **2016**, 15, 1100.

[44]   L. R. Meza, S. Das, J. R. Greer, *Science* **2014**, 345, 1322.

This work presents a conceptually novel hollow-truss microlattice metamaterial capable of harnessing dual sound dissipation mechanisms to achieve superiorly enhanced broadband, and/or customizable sound absorption. A new theorem for the underlying mechanism, based on the superimposed critically coupled acoustic impedances, is brought forward. The performance gain is remarkable considering it comes with a material subtraction as opposed to an addition.

Xinwei Li, Xiang Yu, Wei Zhai*

Less is more: Hollow-truss microlattice metamaterials with dual sound dissipation mechanisms and enhanced absorption capabilities